

Spiral-driven accretion in protoplanetary discs - III tri-dimensional simulations

Patrick Hennebelle^{1,2}, Geoffroy Lesur^{3,4}, Sébastien Fromang¹

¹ Laboratoire AIM, Paris-Saclay, CEA/IRFU/SAP - CNRS - Université Paris Diderot, 91191, Gif-sur-Yvette Cedex, France

² LERMA (UMR CNRS 8112), Ecole Normale Supérieure, 75231 Paris Cedex, France

³ Univ. Grenoble Alpes, IPAG, 38000, Grenoble, France

⁴ CNRS, IPAG, F-38000 Grenoble, France

Preprint online version: November 23, 2016

ABSTRACT

Context. Understanding how accretion proceeds in proto-planetary discs and more generally their dynamics is a crucial issue for explaining the conditions in which planets form.

Aims. The role that accretion of gas from the surrounding molecular cloud onto the disc may have on its structure needs to be quantified.

Methods. We perform tri-dimensional simulations using the Cartesian AMR code RAMSES of an accretion disc subject to infalling material.

Results. For the aspect ratio of $H/R \simeq 0.15$ and disk mass $M_d \simeq 10^{-2} M_\odot$ used in our study, we find that for typical accretion rates on the order of a few $10^{-7} M_\odot \text{ yr}^{-1}$, values of the α parameter as high as a few 10^{-3} are inferred. The mass that is accreted in the inner part of the disc is typically at least 50% of the total mass that has been accreted onto the disc.

Conclusions. Our results suggest that external accretion of gas at moderate values, onto circumstellar discs may trigger prominent spiral arms, reminiscent of recent observations made with various instruments, and lead to significant transport through the disc. If confirmed from observational studies, such accretion may therefore influence disc evolution.

Key words. accretion disc – Instabilities – hydrodynamics

1. Introduction

Accretion discs are ubiquitous in astrophysics as they are observed around stars and black holes and as such they have received considerable attention. In particular it is widely admitted that local instabilities such as the magneto-rotational instability (MRI, e.g. Balbus 2003) or the gravitational instability (e.g. Lodato & Rice 2004) are responsible within different contexts for triggering the transport of angular momentum and mass. The conditions under which these mechanisms may actually work remain debated, for example it is not clear that protostellar discs are sufficiently ionized for the MRI to operate efficiently (e.g. Lesur et al. 2014; Turner et al. 2014).

Mass transferring binary systems are a well studied type of disc and it has early been recognized that the spiral shocks induced by the presence of the companion and the accretion is a source of external disturbances, which can trigger significant accretion within the disc (Sprituit 1987; Larson 1990; Vishniac & Diamond 1989). This has been confirmed by a series of numerical simulations (Sawada et al. 1987; Spruit et al. 1987; Rozyczka & Spruit 1993; Yukawa et al. 1997). In their recent study, Ju et al. (2016) considered the impact of spiral shocks in the presence of MRI turbulence and concluded that the former are playing a significant role also in this context.

On the contrary, most studies have been studying protoplanetary discs in isolation. This is because it is not clear yet whether these objects are still subject to infall from their surrounding parent molecular cloud. A notable exception regards the studies which have addressed the question of disc formation out of their parent dense cores. The newly formed discs are usually massive, self-gravitating and often strongly magnetized and it is generally admitted that angular momentum can be transported by the gravitational torque or by magnetic braking (e.g. Vorobyov & Basu 2008; Machida et al. 2010; Joos et al. 2012; Li et al. 2013; Vorobyov et al. 2015; Masson et al. 2016). For example Vorobyov et al. (2015) performed a series of bidimensional studies of self-gravitating and viscous discs embedded into their parent cores and show that the infall of material has a drastic impact on their evolution. In particular, the angular momentum of the infalling material, appears to be particularly important on the evolution.

To investigate specifically the role that infall may have on the disc, Lesur et al. (2015) performed bidimensional hydrodynamical simulations. They found that infall induces high values of α in the outer part of the disc and smaller but non negligible values, on the order of a few 10^{-4} for an imposed accretion rate of about $10^{-7} M_\odot \text{ yr}^{-1}$ in the inner part of the disc where a plateau of constant α seems to be reached. It has also been shown that although slightly less efficient than non axisymmetric inflows, axisymmetric

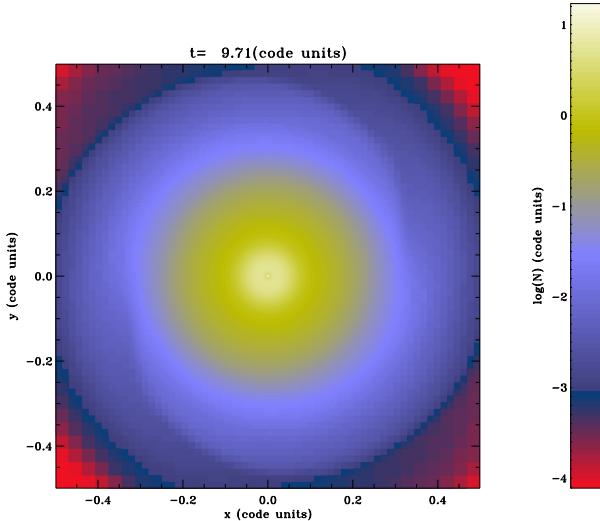


Fig. 1. No accretion case. Column density map. The disc has a radius of about $r = 0.25$.

flows, quickly break up forming a spiral pattern and trigger even smaller scale unstationary structures within the disc.

It is now necessary to investigate this issue in three dimensions, and for that purpose we present here tridimensional numerical simulations of a disc subject to in-fall. Magnetic field and self-gravity are explicitly neglected at this stage. The second section of the paper describes the numerical setup, including initial and boundary conditions. It also presents a simulation of a non-accreting disc which allows us to assess the initial conditions and the effect of numerical viscosity. In the third section, we present in detail a simulation and we study the influence of numerical resolution. We provide some qualitative comparisons with previous analytical works. The influence of the strength of the accretion and quantitative comparison with bidimensional simulations are provided in the fourth section. The influence of the geometry of the accretion flows as well as of the amount of angular momentum it carries is presented in the fifth section. Section six provides some discussions making the link with recent observations of spiral patterns in transitional discs and their interpretation. The seventh section concludes the paper.

2. Tridimensional simulations: setup, resolution and runs performed

We now turn to the description of the series of 3-dimensional simulations that we performed. In a companion paper (Lesur et al. 2015), we presented a series of 2-dimensional runs.

2.1. General setup

2.1.1. Code

To perform our simulations, we employ the code RAMSES (Teyssier 2002), which is an adaptive mesh refinement code working in Cartesian geometry and using finite volume methods and Godunov solvers. Cylindrical or spherical ge-

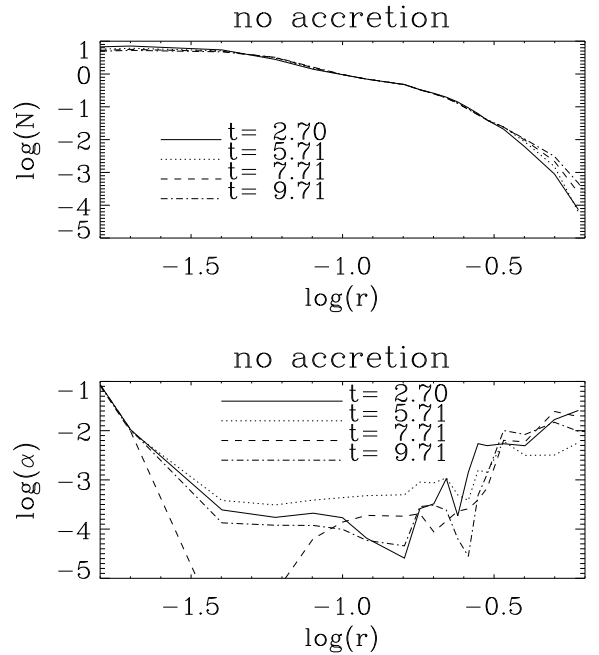


Fig. 2. No accretion case. Column density (top panel) and α value (bottom panel) as a function of the radius r . Typical variations remains limited and the α values are below 10^{-3} rapidly falling below 3×10^{-4} . Note that at small radii ($\log(r) < -1.6$), α increases to high values because of low resolution.

ometries have been traditionally used in the context of disc studies because they ensure exact conservation of angular momentum. This is also the choice which has been made for the simulations presented in Lesur et al. (2015). However, these geometries also introduce singularities along the z -axis or at the origin, that requires specific treatments, while Cartesian codes do not present such a difficulty.

2.1.2. Initial conditions

The initial state is an axisymmetric equilibrium between gravitational, centrifugal and pressure forces. We adopt the locally isothermal approximation,

$$C_s = C_s^0 \times \left(\frac{r}{r_d} \right)^{-1/2}, \quad (1)$$

where r is the cylindrical radius and C_s is the sound speed with $C_s^0 = \sqrt{0.1}$. This approximation is supported by detailed models of discs (D'Alessio et al. 1998; Armitage 2011) temperature structure which in particular show that the dominant source of heating above 2 AU is due to the star irradiation. The mass of the central star is $M_* = 1$ and the disc radius is equal to $r_d = 1/4 = L_b/8$ where $L_b = 2$ is the size of the computational box. This choice ensures that the size of the disc is sufficiently small with respect to the computational box size, in such a way that it is not significantly influenced by boundary conditions. Below only the central part of the computational box is displayed. Therefore the disc occupies initially half of the image displayed. In these units, G , the gravitational constant is equal to 1. This ensures that in the radial direction the gravitational force is always 10 times larger than the

pressure one. The disc aspect ratio is given by

$$\frac{h}{r} \simeq \frac{C_s}{r\Omega} = \frac{C_s^0 \times (r_d)^{1/2}}{\sqrt{GM_*}} \simeq 0.15, \quad (2)$$

where we used $\Omega \simeq r^{-3/2}$ (since $M_* = 1$ and $G = 1$). With this choice, the aspect ratio is therefore constant and equal to about 0.15.

Solving for the axial mechanical equilibrium, we obtain the density profile:

$$\rho = \rho_c(r) \exp \left(\frac{GM_*}{C_s^2} \left(\frac{1}{\sqrt{r^2 + z^2}} - \frac{1}{r} \right) \right), \quad (3)$$

where ρ_c is a free function of r that we have chosen to be equal to

$$\rho_c(r) = \frac{\rho_c^0}{(r/r_d)^{2.5}}. \quad (4)$$

The rotation curve is then simply obtained by requiring mechanical equilibrium in the radial direction

$$\Omega^2 = \frac{\partial_r (C_s^2 \rho)}{r\rho} + \frac{GM_*}{(r^2 + z^2)^{3/2}} \quad (5)$$

The equilibrium solution is truncated at r_d where the density is decreased to a value one hundred times lower. This causes the disc to expand initially. However, as shown below the effect remains limited even in the absence of any external accretion.

The orbital time at the initial disc external radius, r_d , is simply given by

$$\tau_d = \frac{2\pi}{\Omega} = \frac{2\pi r_d^{3/2}}{GM_*} = \frac{\pi}{4} \simeq 0.78. \quad (6)$$

This will constitute the natural time units for the simulation results to which we will refer.

2.1.3. Inner boundary conditions

The central star is placed at the center of the grid and the corresponding gravitational force is directly added to the gas smoothing the r^{-2} dependence within a few computing cells. There is no sink of matter associated and therefore the gas is simply pilling up at the vicinity of the star as the simulation evolves. Around the central star, mesh effects are very important and the flow structure is much affected by the numerical resolution. As quantitatively discussed later, this is only at a certain distance from the central object that the results can be considered as meaningful.

The sound speed dependence, as stated by Eq. (1), leads to a singular behaviour near the z -axis. This creates spurious behaviours and leads to large velocities, which spoil the disc equilibrium. Therefore we have modified the sound speed at small radii, r . We essentially impose that below a radius $r_d/10$, the temperature is simply constant and equal to the value it has at this radius. Since as described below, numerical resolution drops at high altitude, we also make the radius inside which the temperature remains constant, slowly increasing with height, giving it a parabolic shape.

2.1.4. Outer boundary conditions

Since Cartesian coordinates are employed, the computational domain is a cubic box which causes important boundary effects. This would typically cause strong reflections and spurious $m = 4$ modes that affect the disc structure. To avoid these artefacts, the size of the disc has been chosen to represent only 1/4 of the whole box size as mentioned above, which is possible thanks to the AMR scheme of RAMSES. However, although it helps to reduce these effect, we find that they are still significant. Therefore we impose at every timestep a uniform density and a Keplerian velocity for every cell located at $r > 0.9$ (since the box size is $L_b = 2$, the boundary cells in the equatorial plan are located between $r = 1$ and $\sqrt{2}$) from the box center. With this boundary condition, we found that in the absence of infall the flow remains sufficiently symmetrical as shown by Fig. 1.

2.1.5. Numerical resolution

To perform our calculations efficiently we took advantage of the AMR scheme by using a coarse resolution outside the disc, that is to say at radius $r > r_d = 1/4$ and height larger than $z > r_d/2$, while using a finer resolution inside the disc. For most of the runs, the resolution employed the AMR level, $l = 10$ inside the disc implying that the disc radius is described by 128 cells and the whole disc lays in a box of $256 \times 256 \times 128$ cells. As discussed above, the aspect ratio of the disc is about 0.15. Therefore at the disc radius, the disc scale height is described by about 40 cells. At a radius of $r = r_d/10$, this number becomes equal to only 4 cells in a typical scale height. These simulations therefore can tackle a range of radius on the order of $\simeq 5$ -10. Later we refer to this resolution as "standard".

To investigate the issue of numerical resolution, we have also performed runs with a higher resolution in the inner part. The area located at $r < 0.5 \times r_d$ is described using level $l = 11$ implying that at $r = r_d/10$, the scale height is described by about 8 cells. We refer to this resolution as "high". Note that at the same time, the radius at which the gas becomes isothermal has also been reduced by a factor 2.

For all simulations, above the disc radius, r_d the resolution drops to level $l = 8$. Then at radius $r > 1.4r_d = 0.35$ it drops to level $l = 7$ and then at $r > 2r_d = 0.5$, to $l = 6$.

Typically the simulations request about 10,000 (for the "standard" resolution) to about 100,000 cpu hours (for "high" resolution).

2.1.6. The accretion flow

To describe the external accretion, we impose two types of inflow boundary conditions, one axisymmetric and one asymmetrical.

For the asymmetrical accretion scheme, the gas is injected from a circle of radius r_d , contained in the (y, z) plane, and centered in $x = -3.5r_d$, $y = 0$, $z = 0$ at a radial velocity U_{acc} and with a density ρ_{acc} . The accreted gas possesses a specific angular momentum that is equal to either 0 or to $r_d^2 \Omega(r_d)$, that is to say the angular momentum which corresponds to the keplerian velocity at the disc radius, r_d . The accretion velocity is expressed as a function of the sound speed at the boundary, which is equal to

$C_s = C_s^0/2$. The accretion rate is thus given by

$$\dot{M} = \pi r_d^2 U_0 \frac{C_s^0}{2} \rho_{acc}. \quad (7)$$

For the axisymmetrical accretion scheme, the gas is injected from a ring of radius $3.5r_d$ and half thickness r_d . While the value of ρ_{acc} is unchanged, the values of U_{acc} are adjusted in such a way that the total accretion rate is identical to the asymmetrical case

$$\dot{M} = 2\pi(3.5r_d) \times (2r_d) \frac{U_0}{2 \times 2 \times 3.5} \frac{C_s^0}{2} \rho_{acc}. \quad (8)$$

Thus for given values of ρ_{acc} and U_0 , the value of \dot{M} is identical for the two geometries.

Below we consider values of $U_0 = 0.5$ and 2 . To determine typical values of ρ_{acc} , we must refer to observational case. We believe that an efficient way to characterize external infall in accretion discs is given by the dimensionless number, P ,

$$P = \frac{2\pi\dot{M}}{M_d\Omega(r_d)} = \frac{\dot{M}\tau_d}{M_d}, \quad (9)$$

that is to say the ratio between the mass accreted (within the computing box) over one orbital period at $r = r_d$ and the disk mass. This parameter describes the rapidity at which mass is delivered into the disc per disc mass and typical disc timescale.

For a typical T-tauri star of $1 M_\odot$ and a radius $r_d = 100$ AU, accretion rates onto the central star, \dot{M}_{acc} , on the order of up to $10^{-7} M_\odot \text{ yr}^{-1}$ have been inferred (Muzerolle et al. 2005). If we assume that accretion onto the star is a consequence of external infall onto the disc, this suggests that the two accretion rates should be related maybe comparable. In the case of our simulations, with these numbers we have

$$P = \frac{2\pi\dot{M}}{M_d\Omega(r_d)} \simeq 10^{-2} \frac{\dot{M}}{10^{-7} M_\odot \text{ yr}^{-1}} \times \left(\frac{M_d}{10^{-2} M_\odot} \right)^{-1} \left(\frac{M_*}{1 M_\odot} \right)^{-1/2} \left(\frac{r_d}{100 \text{ AU}} \right)^{3/2}. \quad (10)$$

With the density profile stated by Eq. (3) and $\rho_c^0 = 1$, the mass of the disc initially is about 0.1 . Since $r_d = 1/4$, we find

$$P = \frac{2\pi\dot{M}}{M_d\Omega(r_d)} = \frac{\pi^2 C_s^0 r_d^{7/2}}{M_d} U_0 \rho_{acc} \simeq 2 \times 10^{-2} U_0 \frac{\rho_{acc}}{0.1}. \quad (11)$$

In the following, we will adopt $\rho_{acc} = 0.1$. We typically integrate during about 15 orbits at the outer radius. At $r_d/10$, it roughly corresponds to about 500 orbits. During this amount of time and for the value $U_0 = 2$, the total mass inside the computational box increases by about 30%. We stress however, that the increase of the disc mass, that is to say inside the radius, r_d , is 3-4 times lower than this value. This means that the effective mass flux, which falls into the disc is 3-4 times lower than the analytical value stated by Eq. (7). This is because most of the mass added in the computational box piles up in the external medium where the density is low initially.

label	accret	U_0	ρ_{acc}	P	V_0	resolution
NA	no	0	0	0	-	standard
ASR2	a	2	0.1	0.04	1	standard
ASR2h	a	2	0.1	0.04	1	high
ASR0.5h	a	0.5	0.1	0.01	1	high
SR2	s	2	0.1	0.04	1	standard
ASNR	a	2	0.1	0.04	0	standard

Table 1. Summary of the different runs performed in the paper. accret 'a' means asymmetrical accretion while 's' means symmetrical. U_0 is the value of the accretion speed and ρ_{acc} the accretion density (see Eq. 7). P is the accretion parameter (see Eq. 9). V_0 is the rotation velocity of the accretion flow. The standard and high resolution are described in the text.

2.2. Runs performed

Table 1 summarizes the runs performed in the paper and provides consistent labels. This set of simulations attempts to explore the influence of parameters regarding the accretion flow (velocity, density, symmetry and angular momentum), and the numerical resolution.

As can be seen the smallest value of P is 10^{-2} , which for a $10^{-2} M_\odot$ disc and a $1 M_\odot$ star corresponds to an accretion of about $10^{-7} M_\odot \text{ s}^{-1}$. This corresponds to somewhat large values of accretion rate but as explained below, the effective accretion rate onto the disc is typically 3-4 smaller than this value. Note that reducing further the accretion rate would be difficult as numerical resolution (see Fig. 2) is putting constraints on the smallest flux that can be modelled.

2.3. The non-accreting case

As it is important to understand the limits of the numerical experiment we perform, we have first carried out a run without accretion. Figure 1 shows a column density map at time 9.71 (recalling that the orbital time at the disc outer edge is about 0.75 this means that the disc has performed about 14 orbits). The disc remains smooth and symmetrical. There is a weak $m = 2$ pattern located near the disc radius $r = 0.25$. This is likely a consequence of the change of resolution there and the Cartesian mesh. The resulting column density, which is displayed in the top panel of Fig. 2 at 4 timesteps, does not evolve very significantly. It slightly diminishes in the inner part below $r < 0.03$ because of the numerical resolution that becomes insufficient at small radius (see discussion in Sect. 2.1.5). It also increases in the outer part at radii larger than $r > 0.3$, that is to say close to the disc radius. This is expected since the gas is initially out of equilibrium there. Overall these effects remains fairly limited. We also computed the azimuthally averaged α parameter defined as

$$\alpha = \frac{\langle \rho \delta u_r \delta u_\phi \rangle}{\langle P \rangle}. \quad (12)$$

where δu_r and δu_ϕ are the fluctuation of radial and azimuthal velocities. It is displayed in the bottom panel of Fig. 2. After 3-4 orbits, it is below 10^{-3} for radius $0.03 < r < 0.3$, that is to say inside the disc but sufficiently far from the center. After 8-10 orbits, it has dropped further reaching values close to 10^{-4} almost everywhere in the disc. At small radii, $r < 0.03$, we see that α increases to large values. This is clearly a consequence of the insufficient nu-

merical resolution and is consistent with the column density variations.

We conclude that the numerical setup we use, permits us to investigate physical effects, which leads to transport characterized by α larger than 10^{-4} or so in a region located between the disc radius, r_d , and about $r_d/5$. As reported below, this will indeed be the case for the choice of parameters, namely the external accretion rate, that will be considered.

3. Results for non-axisymmetric accretion of rotating gas

3.1. Qualitative description

In this section, we present in detail the simulation labelled as ASR2. It presents a non-axisymmetric accretion flow, which contains the same amount of angular momentum as the gas at the disc outer edge. It has an accretion parameter, P , that is about 4×10^{-2} . Figure 3 shows column density maps at 3 timesteps (from about 4 to 15 orbits) and at two different resolutions (left panels: standard resolution, right panels: high resolution). Top panel shows various noticeable features. First of all, there is a prominent nearly stationary spiral arm going from $x = -0.5$, $y = 0$ to the disc. This is due to the incoming flow, which shocks onto the gas present within the computational box (see further discussion in Sect. 6.1). This triggers the development of a prominent dense spiral arm within the disc, starting at about $x = -0.2$ and $y = 0.15$. Second, there is a second spiral arm that is slightly less prominent and more or less symmetrical to the first one. Because of the gas distribution around the disc being not symmetrical, the whole disc is clearly not symmetrical indicating that $m = 1$ perturbations have been developing. This is at stark contrast with the non-accreting disc presented in Fig. 1.

The middle and bottom panels show later times. Clearly, the spiral patterns developed further and have propagated away reaching radius comparable to a few times the disc radius. This is reminiscent of the very prominent spiral pattern observed in numerical simulations of disc forming in class-0 protostars (e.g. Joos et al. 2012) and suggest that large scales spiral patterns are a natural outcome of externally accreting discs.

3.2. Accreted mass and α parameter

To quantify the transport of mass, that results from the large asymmetry induced by the incoming flow, we have computed the cumulated mass through the disc at various timesteps as well as the mean α parameter.

Bottom panel of Fig. 4 shows the cumulated mass (that is to say the mass contained within a cylinder of radius r) difference between a reference time (first timestep quoted in the figure) and 4 later timesteps, divided by the total mass within the box at the reference time (which is close to the mass within the disc). The four curves show similar features. First, the cumulated mass rapidly increases with radius in the region located outside the disc radius, $r > r_d$. There is a clear break located approximately at the disc radius, $r_d \simeq 0.25$ below which the cumulated mass varies less stiffly with radius. At $\log(r) \simeq -1.2$, the cumulated mass remains constant with time, implying that no mass is crossing this region. Below this radius, the cumulated

mass difference slightly decreases with time implying that the gas there is getting transported outwards (but not further than $\log(r) \simeq -1.2$ where the difference in cumulated mass vanishes). This limit likely represents the point above which the simulation results are dominated by grid effects as anticipated in Sect. 2.1.5.

The α parameter is plotted in the top panel of Fig. 4. The general behaviour is similar to the no-accretion case (Fig. 2), α is large in the very inner part, because of insufficient resolution, and in the disc outer part, where the external material is falling in. At intermediate radius, there is however a plateau with values that increase with time to reach about 10^{-2} . Since this value is about 30 times larger than the values obtained in the non-accretion case, this clearly shows that infall is responsible for the measured α .

3.3. The issue of numerical convergence

To verify the reliability of these simulations, we have performed higher resolution simulations. The right panels of Fig. 3 display the column density map at 3 timesteps. Very similar pattern can be observed for the 2 resolutions, seemingly indicating that the simulations are not dominated by insufficient resolution effects inside the disc.

More quantitative comparisons are given in Fig. 4 where the right panels present the high resolution run (ASR2h). The values of α displayed are similar although run ASR2 indicates slightly larger α at radius, $r < 0.1$. The cumulated mass shown at the bottom panels of Fig. 4 is very similar in the outer part, that is outside the disc ($r > 0.25$). The profile are however more different inside the disc. In particular, the cumulated mass vanishes at smaller radii for ASR2h than for ASR2. The profile of the former is also flatter than the one of the latter. This is clearly an impact of the resolution and this suggests that the limited resolution prevents accretion up to the center.

Altogether these results suggest that accretion triggered by the external flow is able to penetrate significantly inside the disc probably at least down to a radius equal to $\simeq r_d/5$, this number reflecting however the limit set by the highest resolution we could achieve. Typically, we find that with the present configuration, roughly 11% of the mass that has been injected in the box is accreted inside the disc at a radius below $r_d/2$. At a radius below r_d , this number can be larger than 20%, though defining the disc boundary is arbitrary because of the complexity of the flow in this region. This indicates that roughly 50% of the mass that is captured by the disc is able to penetrate at radius smaller than $r_d/2$.

3.4. Comparison between analytical and numerical solutions

In an attempt to better understand the physical mechanism responsible for the transport of mass and angular momentum in the disc through the spiral driven accretion, self-similar solutions in the r variables, have been studied in Hennebelle et al. (2016) following the approach of Spruit (1987). These exact solutions of the inviscid fluid equations depend on the ϕ variable, the polar angle, and present two essential features. First of all they undergo shocks which play an essential role since this is where energy is dissipated, an essential feature for a system that transports angular momentum. Second, the radial velocity is changing

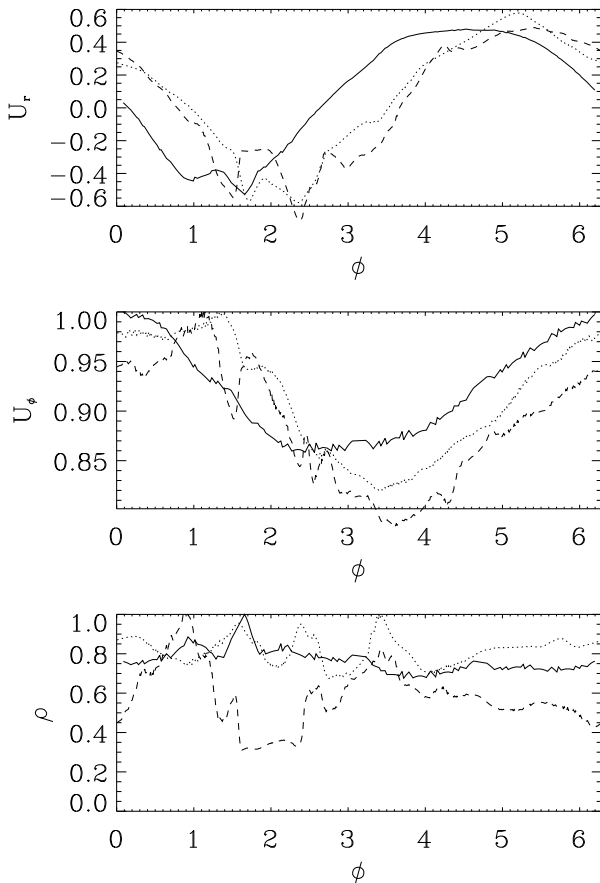


Fig. 5. Azimuthal profiles from simulation ASR2h at time $t = 0.75$ and at radius $r = 0.08$ (solid line), 0.14 (dotted), 0.18 (dashed). Note that the density and the azimuthal velocity have been normalised such that their peak value is equal to 1.

sign with ϕ . This implies that there are both inward and outward mass fluxes. In particular the latter is responsible for the outward flux of angular momentum.

While self-similar solutions remain restricted by the heavy assumptions regarding their dependence, these two aspects constitute essential predictions that should be generic for any accretion discs driven by spiral waves, particularly in the absence of other forces such as self-gravity and magnetic field, which could exert a torque on the gas. To verify whether these features are indeed playing a role in the present simulations, Fig. 5 shows the azimuthal profiles of U_r , U_ϕ and ρ at three different radii. As can be seen the profiles present some similarities with the self-similar solutions. In particular, the radial velocity, U_r is clearly changing sign. It remains negative in about one third of the angular distance and positive for the rest. Moreover there are clear discontinuities, seen both in U_r and U_ϕ which are similar to the shocks of the self-similar solutions (see Fig. 1 of Hennebelle et al. (2016)). Unsurprisingly, there are also significant differences. First, the dominant mode is the $m = 1$ one, a clear consequence of the accretion pattern, which is also $m = 1$. No analytical solution was found for the $m = 1$ case. Second, there are multiple shock features instead of one. Finally, the density fields present more structure in the numerical simulations than in the analytical solutions.

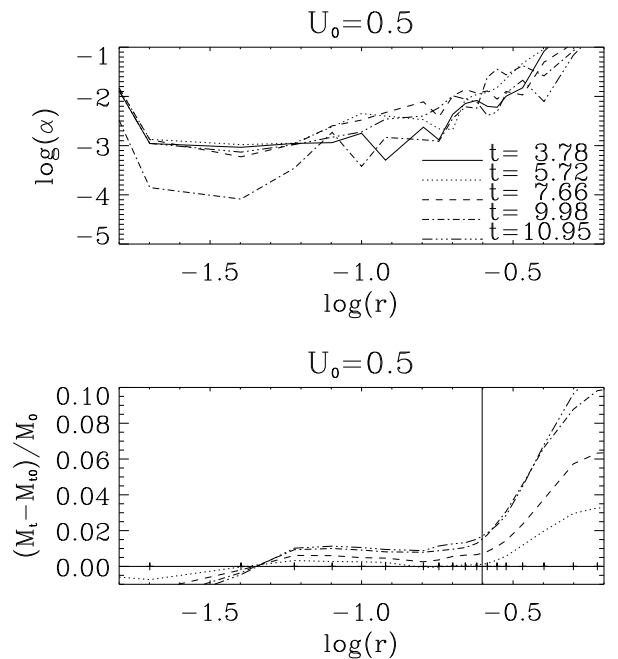


Fig. 6. Simulations ASR0.5h. α values and cumulated mass difference as a function of radius, r .

These differences are likely consequences of the unstationary nature of the numerical solutions.

4. Dependence on infall rate and comparison with bidimensional simulations

4.1. Dependence on infall rate

To investigate the influence that infall has on the disc dynamics, we show a smaller accretion rate characterized by an infall velocity equal to $U_0 = 0.5$. As shown by Eqs. (10)-(11) this corresponds to an accretion rate inside the computation box of about $10^{-7} M_\odot \text{ yr}^{-1}$. The effective accretion rate for the disc is $\simeq 5$ times smaller since as already explained most of the mass does not fall into the disc and remains in the surrounding region. The corresponding α profile and cumulative mass distribution are shown in Fig. 6. The values of α vary from a few 10^{-3} at $\log r = -0.9$ to about 10^{-3} at $\log r = -1.3$ at time 10.95. Note that these values fluctuate in particular at time 9.98 where they are typically 2 times smaller (for $\log r > -1.3$). For comparison the α values for $U_0 = 2$ are about 4 times larger with values on the order of 5×10^{-3} at $\log r = -1.3$ and almost 10^{-2} at $\log r = -0.9$.

As expected, the cumulated mass is also lower with $U_0 = 0.5$. Its value at time 10.95 and at radii $\log r = -0.9$ is about 1.5×10^{-3} while at similar time and radius it is about 5.5×10^{-3} for $U_0 = 4$, that is to say roughly 4 times larger. The mass accreted inside the disc (at $\log r < -1$) is about 20% of the total mass injected in the computational box. Interestingly, we see that the profile of the cumulated mass is fairly flat indicating that most of the mass accreted within the disc is transferred inwards.

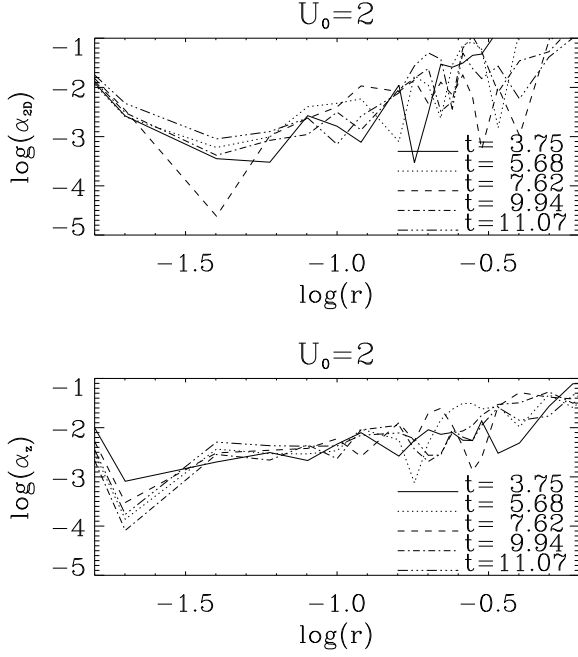


Fig. 7. Values of α_{2D} (obtained by averaging all quantities along the z -axis) and α_z (the difference of α and α_{2D} representing the contribution of the fluctuations along z) for run ASR2h. The two quantities have comparable values in the inner part of the disc.

4.2. Comparison with the 2D simulations

In their 2D simulations, Lesur et al. (2015) estimate that for an accretion rate of $10^{-7} M_{\odot} \text{ yr}^{-1}$, the asymmetrical case with rotation, leads to values of α of about 4×10^{-4} which is therefore 2-3 times lower than the values obtained in our 3D simulations. The same is true for the simulations ASR2h, which corresponds to accretion rate of about $4 \times 10^{-7} M_{\odot} \text{ yr}^{-1}$, as in the 2D case α values slightly below 10^{-3} would be expected (from Fig. 4 of Lesur et al. (2015)). Therefore the 3D simulations performed here present α values about 3 times larger than in the 2D simulations. Further corrections must be taken into account, however. Indeed, Lesur et al. (2015) used an aspect ratio, H/R of 0.1 while the one employed here is 0.15, since from analytical analysis $\alpha \propto (H/R)^{1.5}$ (Hennebelle et al. 2016), the α values in the 3D case may be larger than in the 2D one by a factor of about 1.5-1.6.

4.2.1. Quantifying the importance of 3D effects

To investigate why the typical α values are larger in 3D than in 2D, we have decomposed α in two contributions which represents its bidimensional contribution (α_{2D}) and its remaining 3D contribution due to variation along the z -axis (α_z). To achieve this, we proceed as follows. First, we take the z -averaged quantities defined for example as

$$\bar{u}_r = \frac{\int \rho u_r dz}{\int \rho dz}, \quad (13)$$

Then we can simply calculate an α in 2D as:

$$\alpha_{2D} = \frac{\langle \bar{\rho} \bar{\delta} \bar{u}_r \bar{\delta} \bar{u}_\phi \rangle}{\langle \bar{P} \rangle}. \quad (14)$$

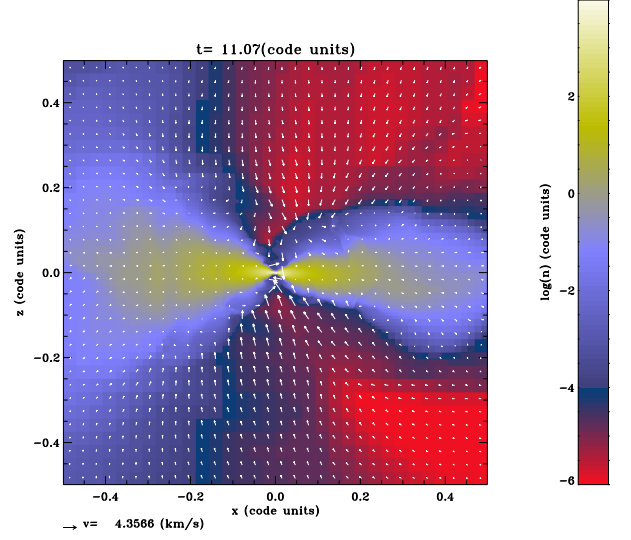


Fig. 8. Density and velocity field in the xz plane of the simulation ASR2. As can be seen accretion is also proceeding from above and below the disc plane along the z -axis.

where the bracket means the averaged values over the radius and azimuth.

Finally, it is easy to show that $\alpha_z = \alpha - \alpha_{2D}$ is equal to

$$\alpha_z = \frac{\langle \rho (u_r - \bar{u}_r)(u_\phi - \bar{u}_\phi) \rangle}{\langle P \rangle}. \quad (15)$$

where the bracket represents the averaged values over radius, azimuth and z -coordinates.

In practice, this is achieved by selecting all cells within bins of radius and azimuthal coordinates. The resulting values of α_{2D} and α_z are displayed in Fig. 7. As can be seen while α_{2D} dominates in the outer part of the disc, they are comparable in the inner part ($\log r < -1$). There is a possible trend of α_z becoming dominant over α_{2D} at small radii.

4.2.2. Physical interpretation

Since it appears that structures along the z -axis are playing a role in producing somewhat larger values of α , Fig. 8 displays the density and velocity fields in the xz plane for the ASR2h simulations. The result is as expected, a significant velocity field is seen in the z -direction and the shape of the disc appears to be irregular and not symmetric. We believe that this latter point is at the origin of the observed difference. Indeed in 3D the gas can enter through the disc directly from above and below instead of inflowing inside the equatorial plane only as in 2D. This certainly produces a higher accretion rate but also is likely to generate more turbulence through accretion since gas that approaches the disc from above undergoes a violent gravitational acceleration along the z -axis and shocks. This infall process likely drives further turbulence.

This could indicate that 2D simulations may generically underestimate the accretion driven turbulence process in accretion discs. Indeed unless the gas temperature varies abruptly inside the disc, the scale height of the accreting gas must be, at least equal, to that of the disc at its outer edge. Thus as the accreting gas is expected to fall onto the disc supersonically, it seems clear that even if approaching

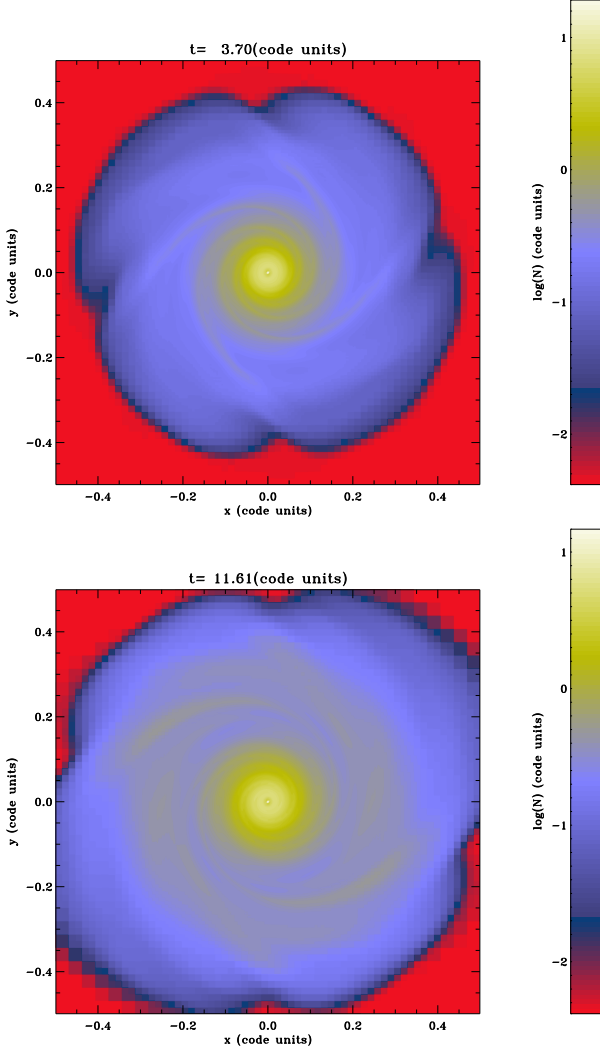


Fig. 9. Simulation SR2 (symmetrical accretion with $U_0 = 2$). Column density map at 2 different timesteps.

the disc close to the equatorial plane, it is not going to pile at the outer disc radius but likely will reach smaller radii from above (bottom).

5. Influence of symmetry and angular momentum

In this last section we briefly explore the impact of other aspect of the accretion flow, namely its symmetry and its angular momentum. Indeed, it is important to remember that the exact way accretion proceeds is not well known as it depends on the whole history of the star formation process. Previous 2D simulations carried out in Lesur et al. (2015) have shown that indeed the accretion rate is not the only parameter to have a significant influence on the disc.

5.1. The axisymmetric case

Figure 9 shows the column density at 2 different timesteps for simulation SR2. It clearly appears that the dominant mode is not the $m = 1$ ones, as is the case for ASR2. Instead the $m = 4$ has developed and became dominant. Note that Cartesian coordinates are likely responsible for the excitation of the $m = 4$ mode. In the 2D axisymmetric simula-

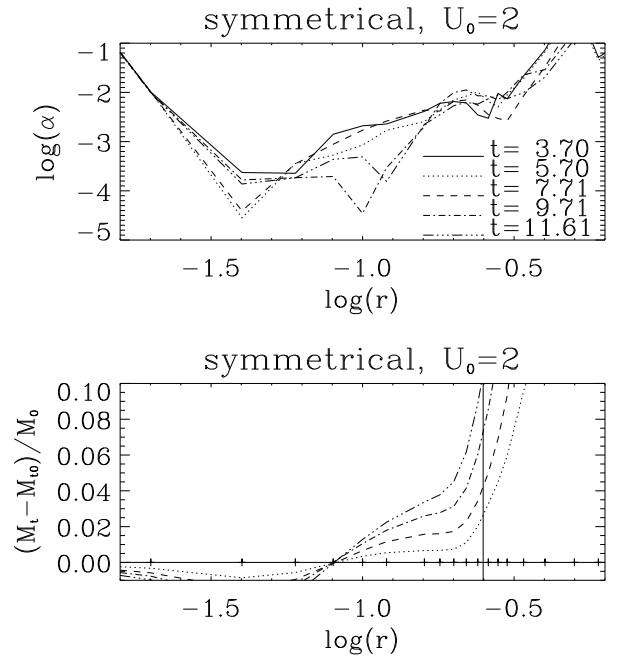


Fig. 10. Symmetrical accretion rate with $U_0 = 2$. α values and cumulated mass difference as a function of radius, r .

tions presented in Lesur et al. (2015), the $m = 4$ mode did not dominate. The spiral wave is tightly wound in the inner part of the disc and more open in the outer part. Let us remind that in Hennebelle et al. (2016), it was shown that the mass and angular momentum fluxes are higher for smaller m . This is a simple consequence of the disc being more axisymmetric for high m .

The α value and the cumulative mass distribution are shown in Fig. 10, they should be compared with simulation ASR2, which has the same resolution (left panel of Fig. 4). It appears that while the α values are comparable in the outer part of the disc ($\log r \simeq -0.6$) to what is obtained for ASR2, they quickly drop in the inner part of the disc reaching almost the floor values inferred from the non-accreting simulation.

This behaviour is in good agreement with the cumulative mass distribution. Indeed while it is as high as in ASR2, in the outer part of the disc it quickly drops in the disc inner part indicating that the mass flux is significantly lower than for ASR2.

5.2. Accretion of non-rotating gas

Finally since angular momentum is another quantity which is playing an important role and whose distribution is not well understood, Fig. 11 presents a calculation in which the accreted gas is injected without angular momentum. As can be seen the impact on the disc is really drastic since its radius shrinks by almost a factor 2. This is because on one hand the centrifugal radius is proportional to j^2 , j being the specific angular momentum, and on the other hand, the specific angular momentum decreases because the total mass increases but not the total angular momentum. At the time corresponding to the second snapshot ($t = 11.62$), the mass in the box has increased by about 40%. Therefore the specific angular momentum has decreased by the same

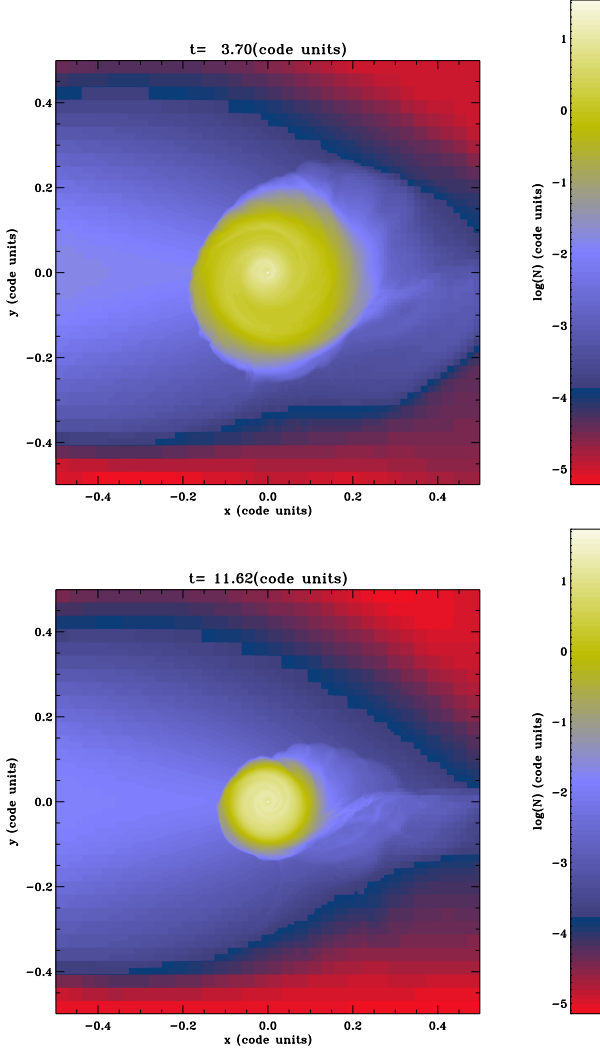


Fig. 11. Simulation ASNR2 (asymmetrical accretion with $U_0 = 2$ and no rotation). Column density map at 2 different timesteps. The disc quickly shrinks in size.

amount and since $1.4^2 \simeq 2$, we get a reasonable agreement. The α values, not been displayed here for conciseness, are also much higher than for the other cases and typically reach around 0.1. Interestingly, although the disc dynamics appears to be rather vigorous, there are no sign of the prominent spiral pattern which develops in ASR2 in the vicinity of the disc. As discussed above we believe that this is due to the absence of rotation within the accreting gas.

These two cases clearly illustrate that the accretion rate is not the only parameter playing a role. There is therefore considerable uncertainty and there may be a broad diversity of situations depending on the real distribution of accretion episode in star formation regions.

6. Discussion

6.1. Interpretations of observations

Many observations of evolved transition discs at various wavelengths from radio to optical, have been carried out in recent years (e.g. Hashimoto et al. 2011; Garufi et al. 2013; Boccaletti et al. 2013; Christiaens et al. 2014;

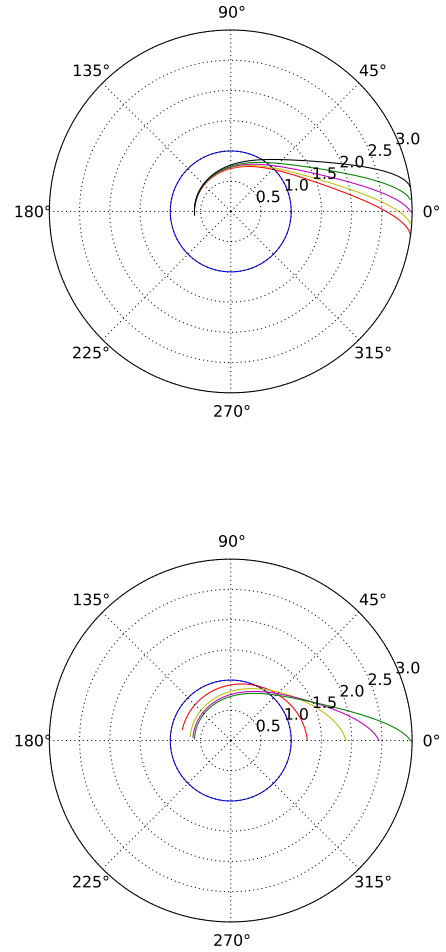


Fig. 12. Elliptical orbits for various particles with same energy but different trajectories mimicking the accretion studied in this paper (top panel) and particles with different energies (specified by $\eta = r_0/r_d$) but same angular momentum. As can be seen the orbits tend to approach or even cross each other which would result in a shock and a spiral arm.

Avenhaus et al. 2014; Wagner et al. 2015; Benisty et al. 2015). They consistently report the presence of density structures such as prominent spiral arms located within or *in the vicinity* of the disc. The origin of these structures remains debated. They have often been attributed to the presence of a massive planet which indeed can excite spiral patterns (e.g. Rafikov 2002; Baruteau et al. 2014). Self-gravity is another mechanism which has been proposed to explain these waves but it is not quite clear that all the discs where spiral patterns are observed are massive enough (see discussion in Hall et al. 2016).

While these explanations are certainly possible, the simulations performed in this work suggest that accretion is another viable mechanism. Indeed, visual inspection and comparison between Fig. 3 and figures such as Fig. 1 of Hashimoto et al. (2011) or Fig. 1 of Benisty et al. (2015) show striking resemblance with clear spiral patterns that tend to open up as they get more distant from the disc.

In the simulation, at least, these spiral features are clearly a consequence of the accretion of rotating gas that is approaching centrifugal equilibrium (let us recall that these spiral arms are absent in the non-rotating accretion case shown in Fig. 11). To understand this more quantitatively let us simply follow a rotating fluid particle that is infalling toward a star. Let us assume that its specific angular momentum, j is conserved and let us ignore all forces but gravity and centrifugal acceleration. Angular momentum conservation and energy conservation lead to

$$v_\phi = \frac{j}{r},$$

$$\frac{1}{2}(v_r^2 + v_\phi^2) - \frac{GM_*}{r} = -\frac{GM_*}{r_0}. \quad (16)$$

Combining them, we can express

$$\frac{v_r}{v_\phi} = \left(2 \left(\frac{r}{r_d} - \frac{r^2}{r_0 r_d} \right) - 1 \right)^{1/2} = \tan \theta, \quad (17)$$

where $r_d = j^2/GM_*$ is the centrifugal radius and where θ is the angle between the stream line and the azimuthal direction. Let us stress that the trajectory are simply Keplerian orbits of various eccentricity. Figure 12 shows five orbits corresponding to the same angular momentum and energy but different trajectories mimicking the accretion used in the simulations presented in this paper (upper panel) and five orbits with different energies (leading to different values of $r_0 = \eta r_d$ where r_d is the Keplerian radius and corresponds to the blue circle) which would result from energy dissipation in the accretion flow (lower panels). The five values of η are 1, 2.1, 2.6, 3.1 and 3.6. Interestingly the orbits get very close to each others and even cross, which would unavoidably result in a shock and a spiral structure. It is tempting to attribute the formation of the prominent spiral structures seen in Fig. 3 to this mechanism. These spirals could therefore be simply nearly kinematic waves (Toomre 1977).

From Eq. (17), we see that typically the stream line makes an angle $\theta \simeq 45^\circ$ just before it enters the disc. This angle increases at larger radii and for example is about 60° at $r = 2r_d$. Note that if energy is not conserved, which is likely the case close to the disc because of the shock then the angle θ is accordingly reduced. Moreover let us stress that the disc radius is not so well determined in particular because the incoming particles are shocking on its surface (compare Figs. 1 and 3), therefore the spiral arm may be able to penetrate “inside” the disc as is the case in Fig. 12 and in simulations ASR2.

If this interpretation of the origin of some of the observed spiral pattern is confirmed, this would constitute a signature of ongoing accretion in transitional discs.

7. Conclusion

We have investigated the influence that infall may have onto low mass circumstellar protoplanetary discs by performing 3D hydrodynamical numerical simulations ignoring self-gravity. The underlying idea, here, is to concentrate only on hydrodynamics in order to disentangle the effects of the different physical processes.

Our results confirm the 2D simulation results presented in Lesur et al. (2015): infall onto the disc has an influence,

even at small radii. For an infall rate inside the computational box of about $4 \times 10^{-7} M_\odot \text{ yr}^{-1}$ (which corresponds to an effective accretion rate onto the disc about 3-4 times smaller), we obtained α values, which inside the disc (that is at radii about 5 times smaller than the disc radius), are as high as 5×10^{-3} when the disk has a mass on the order of $10^{-2} M_\odot$ and a typical thickness $H/R \simeq 0.15$. At the disc outer edge, values of α up to 10^{-1} are obtained. These values decrease with the infall rate and for $10^{-7} M_\odot \text{ yr}^{-1}$ (corresponding to an infall onto the disc about 4 times smaller), we obtain α values typically 3-5 times smaller that is to say equal to about 10^{-3} .

As these α values are a few times larger than the ones that have been measured by Lesur et al. (2015), we have estimated the contribution to α of the vertically averaged flows. The associated stress, α_{2D} , was compared to the quantity $\alpha_z = \alpha - \alpha_{2D}$, which quantifies the transport associated with 3D structures. We found that α_{2D} and α_z have similar values in the inner part of the disc. This suggests that 3D dynamical processes, in particular the fact that the accreted gas can fall into the disc from above and below rather than from the equatorial plane only, is playing a role and produces larger fluctuations. For the conditions that we have been exploring, we found that typically about 10% of the mass injected in the computational box is accreted deep inside the disc (at a radius smaller than half its initial radius). Since the mass which falls effectively into the disc is 3-4 smaller than the mass injected into the box, the mass that is being accreted in the inner part of the disc is about half the mass that effectively falls onto it, though defining the disc boundary accurately appears to be a difficult task.

Finally, we have also explored the influence of the symmetry and the angular momentum of the accreted gas, finding that both have a significant influence on the effects that infall has onto the disc. More symmetrical flows have a more limited influence while slowly rotating material may influence the disc dramatically since it reduces the specific angular momentum. This clearly indicates that precisely quantifying the impact that infall may have on discs requires a detailed knowledge of the star formation process and the nearby environment of the star-disc system.

The accretion of rotating gas, naturally produces prominent spiral patterns both inside and outside the disc. The latter seems to be a natural consequence of spiralling collapsing gas dynamics and largely triggers the spiral pattern within the disc. This pattern presents striking resemblance with recent observations of transitional discs, which may indicate that, at least some of the spirals observed in these objects are due to infalling motions rather than due to the presence of planets.

Acknowledgments This work was granted access to HPC resources of CINES under the allocation x2014047023 made by GENCI (Grand Equipement National de Calcul Intensif). This research has received funding from the European Research Council under the European Community’s Seventh Framework Programme (FP7/2007-2013 Grant Agreement no. 306483).

References

- Armitage, P. J. 2011, ARA&A, 49, 195
- Avenhaus, H., Quanz, S. P., Schmid, H. M., et al. 2014, ApJ, 781, 87

- Balbus, S. A. 2003, *ARA&A*, 41, 555
- Baruteau, C., Crida, A., Paardekooper, S.-J., et al. 2014, *Protostars and Planets VI*, 667
- Benisty, M., Juhasz, A., Boccaletti, A., et al. 2015, *A&A*, 578, L6
- Boccaletti, A., Pantin, E., Lagrange, A.-M., et al. 2013, *A&A*, 560, A20
- Christiaens, V., Casassus, S., Perez, S., van der Plas, G., & Ménard, F. 2014, *ApJ*, 785, L12
- D'Alessio, P., Cantó, J., Calvet, N., & Lizano, S. 1998, *ApJ*, 500, 411
- Garufi, A., Quanz, S. P., Avenhaus, H., et al. 2013, *A&A*, 560, A105
- Hall, C., Forgan, D., Rice, K., et al. 2016, *MNRAS*, 458, 306
- Hashimoto, J., Tamura, M., Muto, T., et al. 2011, *ApJ*, 729, L17
- Hennebelle, P., Lesur, G., & Fromang, S. 2016, *A&A*, 590, A22
- Joos, M., Hennebelle, P., & Ciardi, A. 2012, *A&A*, 543, A128
- Ju, W., Stone, J. M., & Zhu, Z. 2016, *ArXiv e-prints*
- Larson, R. B. 1990, *MNRAS*, 243, 588
- Lesur, G., Hennebelle, P., & Fromang, S. 2015, *A&A*, 582, L9
- Lesur, G., Kunz, M. W., & Fromang, S. 2014, *A&A*, 566, A56
- Li, Z.-Y., Krasnopolsky, R., & Shang, H. 2013, *ApJ*, 774, 82
- Lodato, G. & Rice, W. K. M. 2004, *MNRAS*, 351, 630
- Machida, M. N., Inutsuka, S.-i., & Matsumoto, T. 2010, *ApJ*, 724, 1006
- Masson, J., Chabrier, G., Hennebelle, P., Vaytet, N., & Commerçon, B. 2016, *A&A*, 587, A32
- Muzerolle, J., Luhman, K. L., Briceño, C., Hartmann, L., & Calvet, N. 2005, *ApJ*, 625, 906
- Rafikov, R. R. 2002, *ApJ*, 569, 997
- Rozyczka, M. & Spruit, H. C. 1993, *ApJ*, 417, 677
- Sawada, K., Matsuda, T., Inoue, M., & Hachisu, I. 1987, *MNRAS*, 224, 307
- Spruit, H. C. 1987, *A&A*, 184, 173
- Spruit, H. C., Matsuda, T., Inoue, M., & Sawada, K. 1987, *MNRAS*, 229, 517
- Teyssier, R. 2002, *A&A*, 385, 337
- Toomre, A. 1977, *ARA&A*, 15, 437
- Turner, N. J., Fromang, S., Gammie, C., et al. 2014, *Protostars and Planets VI*, 411
- Vishniac, E. T. & Diamond, P. 1989, *ApJ*, 347, 435
- Vorobyov, E. I. & Basu, S. 2008, *ApJ*, 676, L139
- Vorobyov, E. I., Lin, D. N. C., & Guedel, M. 2015, *A&A*, 573, A5
- Wagner, K., Apai, D., Kasper, M., & Robberto, M. 2015, *ApJ*, 813, L2
- Yukawa, H., Boffin, H. M. J., & Matsuda, T. 1997, *MNRAS*, 292, 321

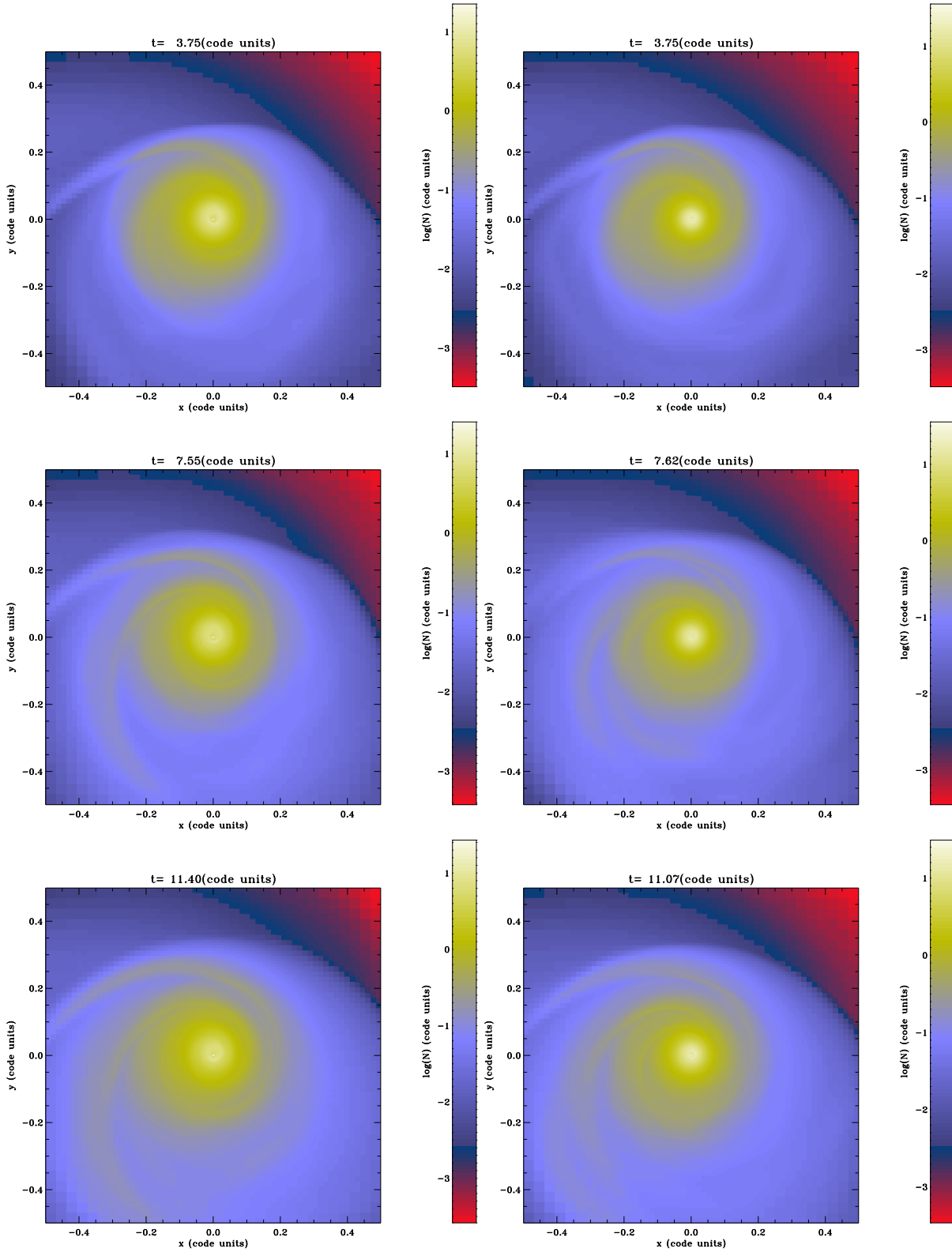


Fig. 3. Simulation ASR2 (asymmetrical accretion with $U_0 = 2$ and standard resolution, left panels) and ASR2h (high resolution, right panels). Column density map at 3 different timesteps. The disc initially has a radius of about $r = 0.25$. Note that the spiral pattern is remarkably stationary.

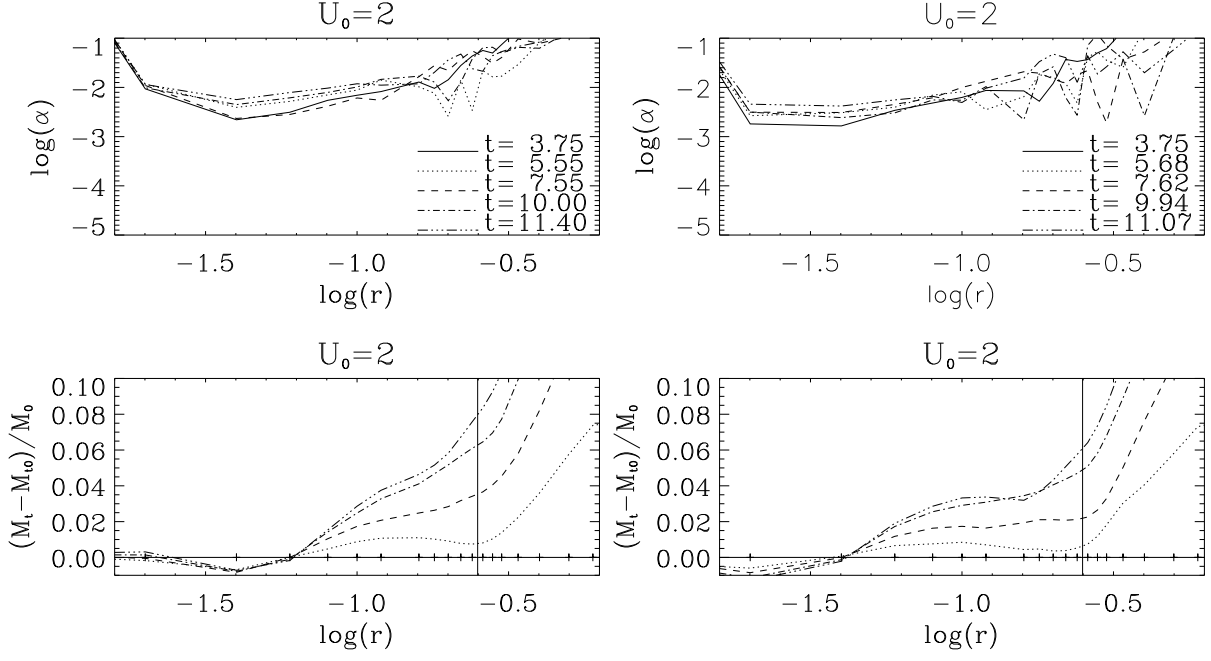


Fig. 4. Simulations ASR2 (left) and ASR2h (right). Top panels: α as a function of the radius r . Bottom panels: cumulated mass difference over total mass (see text). Solid lines at $r = 0.25$ represent the initial disc edge.